Scientific Machine Learning of 2D Perovskite Nanosheet Formation

Jakob C. Dahl,[†,‡,¶] Samuel Niblett,[†,‡,§] Yeongsu Cho,[∥] Xingzhi Wang,[†,‡] Ye Zhang,[†,‡] Emory M. Chan,[¶] and A. Paul Alivisatos[*,†,⊥,‡,#,@]

†Department of Chemistry, University of California, Berkeley, California 94720, United States

‡Materials Sciences Division, Lawrence Berkeley National Laboratory, Berkeley, California 94720, United States

¶Molecular Foundry, Lawrence Berkeley National Laboratory, Berkeley, California 94720, United States

§Yusuf Hamied Department of Chemistry, University of Cambridge, Lensfield Road, Cambridge CB2 1EW, United Kingdom

∥Department of Chemistry, Columbia University, New York, New York 10027, United States

⊥Department of Materials Science and Engineering, University of California, Berkeley, California 94720, United States

#Kavli Energy NanoScience Institute, Berkeley, California 94720, United States

@Current Affiliation: Department of Chemistry, University of Chicago, Chicago, Illinois 60637, United States

E-mail: paul.alivisatos@uchicago.edu

Abstract

We apply a scientific machine learning framework to aid the prediction and understanding of nanomaterial formation processes via a joint spectral-kinetic model. We apply this framework to study nucleation and growth of 2D perovskite nanosheets. Colloidal nanomaterials have size-dependent optical properties, and can be observed in situ, all of which make them a good model for understanding the complex processes of nucleation, growth and phase transformation of 2D perovskites. Our results demonstrate that this model nanomaterial can form through two processes at the nanoscale: either via a layer-by-layer chemical exfoliation process from lead bromide nanocrystals or via direct nucleation from precursors. We utilize a phenomenological kinetic analysis to study the exfoliation process and scientific machine learning to study the direct nucleation and growth, and discuss the circumstances under which it is more appropriate to use phenomenological or more complex machine learning models. Data for both analysis techniques are collected through in-situ spectroscopy in a stopped flow chamber, incorporating over 500,000 spectra taken under more than 100 different conditions. More broadly, our research shows that the ability to utilize and integrate traditional kinetics and machine learning methods will greatly assist the understanding of complex chemical systems.

Introduction

Machine learning (ML) methods hold the promise to predict outcomes in complex chemical systems,[1–3] including nanocrystal synthesis.[4,5] Much recent work has focused on learning reaction outcomes directly from the experimental parameters, essentially treating the synthesis process as a black box, but it is difficult to convert this correlative prediction into physical or mechanistic insight. Since chemical kinetics provides an existing framework for phenomenological modeling of the time dependence of chemical reaction networks, it is rea-

sonable to expect that incorporating this information into an ML method will simplify the learning problem and improve the interpretability of the final model.

Since most complex syntheses, especially of nanoparticles, occur outside the high-temperature thermodynamically-controlled limit, they depend heavily on kinetic processes.[6,7] The time dependence of concentrations for reagents and products is therefore of crucial importance for understanding the progress and dynamics of the reaction. Coupling ML methods to a kinetic model of this time dependence is apromising approach for understanding the synthetic pathway. Physically modeling the kinetics of reactions has long had a distinct place in synthesis science. Linear, or at least analytic,[8] models of reaction kinetics as a function of temperature, concentrations or chemical substituents are part of the standard repertoire that chemists use to investigate how reactions happen. However, many reactions cannot be described by analytically solvable models.[8–10] In particular, connections between different reactions result in coupled differential equations that must be solved numerically. This task can be especially difficult for nanoparticle synthesis, where non-linear processes lead to stiff differential equations.[11,12]

Ideally, complex numerical models of a synthesis reaction network should be parameterised against experimental concentration time series data in order to determine physical parameters, such as rate constants, and explore mechanisms. Techniques utilized in ML offer alternative approaches of efficiently exploring fits to concentration over time, as well as reducing the risk of overfitting through regularization or cross-validation. Improved fitting efficiency may in turn allow the use of more complex models. This approach, sometimes termed scientific machine learning,[13] has been used for a variety of chemical systems,[14,15] and has great potential for application in nanoscale materials chemistry.

We choose to examine the formation of two dimensional perovskite nanosheets of OLA_2PbBr_4, where OLA denotes an oleylammonium ion. This chemical system provides an intriguing model with low dimensionality that is computationally tractable and is of interest both in the 2D materials community[16–18] as well as in the halide perovskite nanocrystal commu-

nity.[19,20] Two-dimensional halide van-der-Waals structures have been studied extensively[21] and exhibit strong quantum confinement that affects dielectric confinement,[22] exciton binding energies, and electron transport,[23] as is the case for other 2D materials.[24] To design these properties at the nanoscale, we need to control the size and shape of the materials. To achieve that control, we need a functional understanding of the formation mechanisms of these structures, which remains a challenge. While there has been some work to understand growth in a thin-film environment,[16–18] the growth in colloidal environments has not been well studied. By utilizing colloidal synthesis techniques, we can achieve high concentrations of early stage nuclei that can be observed through optical absorption spectroscopy, and thus obtain high quality measurements of time-dependent concentrations across the entire reaction sequence. In addition, the 2D exciton peaks in these absorption spectra exhibit a blue shift due to lateral quantum confinement in the smallest nanosheets, which allows us to estimate particle size during early growth. Combining time and concentration information is crucial to creating a useful model for the growth of these OLA_2PbBr_4 nanosheets, providing a suitable test case for our methodology.

Our research connects 2D materials synthesis science with the synthesis of nanocrystals, and of perovskite nanocrystals in particular. Studies of perovskite nanocrystal formation have so far been limited by the absence of kinetic data with sufficient time resolution to resolve nucleation and growth processes.[20] By cooling the reaction down close to room temperature and using stopped flow spectroscopy with millisecond resolution to observe the synthesis, we gather an abundance of absorption spectra resolving the appearance and reaction dynamics of species early in the formation process, resolving open questions from previous studies. Machine learning and automated analysis becomes crucial to interpreting the quantity of data gathered in this way.

Our approach also allows us to test different models of nanocrystal reaction kinetics and physical properties. We investigate the dynamics of the nanosheet formation mechanism through stopped flow experiments of nanocrystal transformation processes and discuss im-

plications for the formation of perovskite nanocrystals more generally. This research may be crucial to understanding the formation of ternary perovskite nanocrystal species, which rapidly form from the binary lead halides through chemical transformations at room temperature.[12,25–28] In particular, the formation route of ternary lead halides appears to be controlled by an equilibrium between solution complexes, 2D perovskite nanosheets, and lead bromide nanocrystals,[12] which explains the success of previous synthesis control strategies.[29–31]

In this article, we outline methods to probe the synthesis of colloidal, single layer 2D perovskites using in-situ stopped flow absorption spectroscopy, which yields time series of spectral information at millisecond resolution. After discussing the results qualitatively, we employ traditional kinetic analysis to understand a lead bromide chemical exfoliation mechanism through which nanosheets can form. Finally, we construct a model of the optical absorption spectrum as a function of size, as well as a model of the kinetic behavior of direct nanosheet nucleation and growth. Through combination of these two models, we enable prediction of the entire stopped flow absorption time series. By fitting these models to experimental data and evaluating extrapolative cross-validation prediction accuracy, we can determine physical parameters of the system and hence shed light on the properties, formation mechanism and synthesis of OLA_2PbBr_4 nanosheets.

Methods

Synthesis

Chemicals and Materials

Dodecane (>99.0%), lead acetate ($PbCH_3COO$, >97.0%), oleylamine (OLA) $\geq$99.0%), oleic acid (OA) $\geq$99.0%) and benzoyl bromide $\geq$99.0%) were purchased from Sigma Aldrich. Hexane (mixed isomers, 98 %) was purchased from Fischer Scientific. All materials were used as received.

Synthesis and Transformation of PbBr$_2$ nanocrystals

Lead Acetate was dissolved in oleic acid, and stock solutions of lead oleate solution were prepared as in previous work.[12] Lead bromide nanocrystals were synthesized by mixing 60 μL lead oleate solution with 60 μL oleic acid and 20 μL oleylamine in a 4 mL vial containing 2 mL of hexanes and a stirbar. At room temperature, 9 μL of benzoyl bromide were added to the mixture, then the solution was stirred for 10 minutes. An equal amount of isopropanol was added to the solution to induce precipitation, then the mixture was centrifuged at 5,000 rpm. The resulting pellet was redispersed in hexanes. A solution of PbBr$_2$ nanocrystals can be transformed to OLA$_2$PbBr$_4$ nanosheets by addition of 2 - 4 equivalents oleylammonium bromide. Characterization of all products is detailed in the SI.

Stopped Flow Experiments

Stopped flow UV-VIS experiments were used to obtain a time series of chemical concentrations during nanoparticle formation under a range of different experimental conditions (i.e. initial concentrations of reagents and temperature). All experiments were performed on an Applied Photophysics SX 20 stopped flow spectrophotometer illuminated by a Xenon lamp and detected with a silicon photodiode array with 256 measurement points spaced at equal distance between 190 and 735 nm. The stopped flow chambers were stored under ethanol, then filled with toluene and emptied three times, then filled with dodecane and emptied three times before measurement. Spectral aquisition times (usually $\sim$ 25 ms) and instrument gain were optimized with dodecane as a solvent to minimize aquisition times while maximizing spectral sensitivity and avoiding detector overflow. A background of dodecane was subtracted internally. Spectra were recorded over 1000 time points, usually for 60 seconds and for no longer than 3600 seconds. The syringes and stopped flow chamber were periodically flushed with ethanol to remove any accidentally deposited material in the measurement chamber, and the same setup procedure was repeated after flushing.

Stock solutions of Br, OLA, OA, Cs-OA and Pb-OA were prepared as in our previous

work,[12] but diluted to 8.5, 3.0, 3.2, 1.0 and 0.66 mM in dodecane, respectively. All stock solutions were added to the syringes used for loading the stopped flow chambers with volumes varying between 10 - 100 μL and mixed with 2 mL dodecane. For synthesis experiments, OLA, OA, and Pb-OA solutions were placed in one syringe and Br solutions were placed in the other syringe. (See Figure 3) For the transformation experiments, a stock solution of lead bromide nanocrystals was prepared at around 1.0 O.D. at 330 nm and placed in the first syringe, while OLA and Br solutions were mixed in the second syringe. Each experiment was performed at least in triplicate for a duration of 60 seconds. Observations in the interval between 420 and 305 nm in which absorption due to lead halide nanoplates and nanocrystals occurs were used for further analysis. Data processing is described in the SI.

Results and discussion

In-Situ Studies of Exfoliation and Synthesis

To observe the formation process of 2D perovskite nanosheets, we utilized stopped flow studies as shown in Figure 1. To initiate the reactions, solutions containing lead oleate, oleylamine and oleic acid were rapidly ($<$ 5 ms) mixed with benzoyl bromide solutions by injecting them into the stopped-flow chamber. We quantified the time-dependent concentrations of lead bromide nanocrystals and 2D perovskite nanosheets through their distinct optical signatures: a shoulder on the absorption peak near 330 nm with an onset at 350 nm represents lead bromide nanocrystals, and 2D perovskite above-bandgap states are represented by an exciton peak around 395 nm along with an absorption band above 370 nm (Figure S1, see also ref[12,32]). These features are marked with dotted lines in Figure 1 A - D. In this figure, each vertical slice is a spectrum, with the height of the spectrum converted to color. The spectra shown here cover over 3 orders of magnitude in time, from 10s of milliseconds to minutes, which allows us to observe and interrogate early stages of reaction kinetics. At low [OLA] to [Pb] ratios, initial formation of PbBr$_2$ nanocrystals is followed
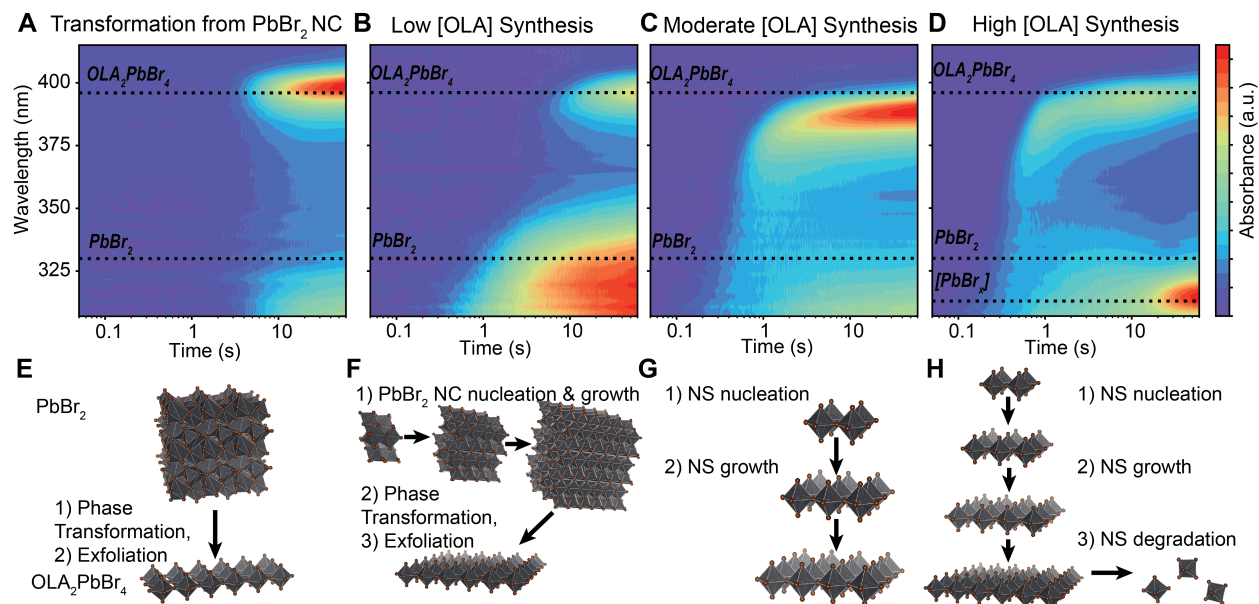
7

Figure 1: *Qualitative Observations in Stopped Flow of OLA_2PbBr_4 Synthesis* and cartoons of the proposed associated mechanisms. A and E) Transformation from $PbBr_2$ nanocrystals. B and F) Synthesis at low OLA concentrations. C and G) Synthesis at intermediate OLA concentrations. D and H) Synthesis at high OLA concentrations. The stopped flow experimental results (A-D) are depicted as 2D contour plots, with time in logarithmic units on the x-axis, wavelength on the y axis and color representing relative absorbance.

by the appearance of $OLA_2 PbBr_4$ absorption peaks at 395 nm (Figure 1 B). Conversely, at high [OLA]/[Pb] values, no $PbBr_2$ formation is observed and the excitonic peak of OLA_2 $PbBr_4$ is initially blue-shifted by 50 nm or 200 meV, gradually shifting to $\sim$ 390 nm over 1 - 20 seconds after the reaction is initiated (Figure 1 C and D). This blueshift most likely indicates lateral quantum confinement, which diminishes over time as the nanosheet grows to larger sizes. These qualitative observations imply that there is a transition between two mechanisms by which 2 D perovskites may be formed in colloidal solution: either through a transformation process from $PbBr_2$ nanocrystals (Figure 1 E, F), or via a direct nucleation and growth pathway (Figure 1 G, H). We have also observed that there appear to be intermediate processes, i.e. transformation from very small $PbBr_2$ nanocrystals to OLA_2PbBr_4 nanosheets, at [OLA]/[Pb] values between those shown in Figure 1 B and C (Figure S3).

To further test and characterize the transformation reaction from $PbBr_2$ nanocrystals, we exposed a solution of previously synthesized $PbBr_2$ nanocrystals to oleylammonium bromide solutions, inducing exfoliation to single layer OLA_2PbBr_4 flakes. Both the nanocrystals and their transformation product were characterized with absorption spectroscopy, XRD, TEM and AFM, and match previously reported information on the proposed species (see Figure S1).[12,32,33] On a qualitative level, what is most apparent is that the characteristic 2D perovskite exciton peak appears immediately above 390 nm, with hardly any observable blueshift at shorter time scales (Figure 1 A), regardless of the initial conditions chosen (Figure S2). This invariance implies that the nanosheets are not laterally confined at any time, i.e. larger structures of OLA_2PbBr_4 (1 ML) nanosheets are formed synchronously rather than from smaller, initially confined nuclei. This is highly suggestive of a chemical exfoliation mechanism (Figure 1 E) rather than dissolution of $PbBr_2$ nanocrystals and renucleation as nanosheets (Figure S2).

To analyze and quantify these two mechanisms, we deliberately chose two different approaches based on the data at hand and the complexity of the system. For the transformation, there are two main chemical species, the $PbBr_2$ nanocrystals and large 1 ML nanoflakes.

9

This system can be approximated as only involving two observed chemical species and their absorption profiles and extinction coefficients are known, so we used traditional kinetic analysis based on the initial rates of reaction to gain further understanding of the mechanism. For the direct nucleation, which involves a series of plates at different sizes for which the exciton peak positions and extinction coefficients are not known, we built a combined model based on kinetic and optical descriptors that incorporates both density functional theory and in-situ data.

Kinetic Analysis of the Activation Energy for 2D Perovskite formation via $PbBr_2$ nanocrystals

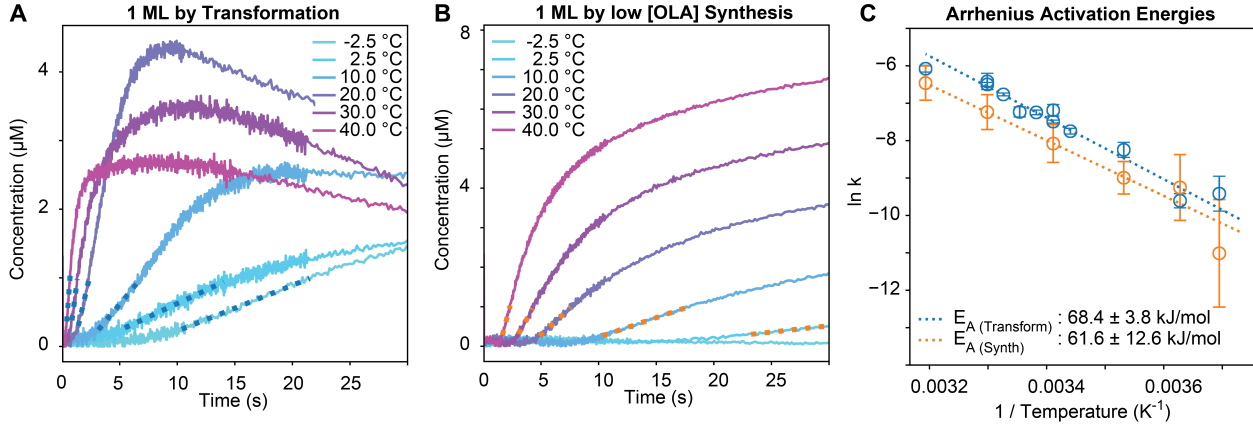Figure 2: *Activation Energy of Transformation* A) Kinetic traces of OLA_2PbBr_4 concentrations formed by exfoliation from pure $PbBr_2$ nanocrystals at different temperatures, with linear initial fits (blue dotted lines). B) Kinetic traces of OLA_2PbBr_4 concentrations in a low OLA concentration synthesis at different temperatures with linear fits (orange dotted lines). C) Arrhenius plot of initial kinetic rates extracted from A (blue squares) and B (orange circles) showing activation energies.

For the traditional kinetic analysis of the transformation of $PbBr_2$ nanocrystals into OLA_2PbBr_4 nanoflakes, we analyzed the rate of appearance of 1 ML during the early parts of the reaction. We extracted the concentrations using a previously described deconvolution algorithm[12] to separate the optical spectrum into relative contributions of different species. This approach was possible for any stopped flow measurement in which we did not observe significant blue-shifts (i.e. experiments which follow the transformation pathway and do not have significantly changed absorption properties), as the algorithm uses peak positions to assign species identity.

Fig. 2 shows the concentrations of nanosheets formed as a function of time at different temperatures and conditions. While there are non-linear dynamics and product degradation at longer times as well as an induction period, the initial linear concentration regime should correspond to the rates of the process most directly involved in the transformation. We

fit these "initial" kinetic rates for a concentration range between 2 and 15% of the final concentration to eliminate any effects from induction periods or degradation observed at longer times in Figure 2 (further discussion of this treatment in the SI). We apply this analysis to both the transformation-only experiments starting from pre-synthesized $PbBr_2$ nanocrystals (Figure 2A) and the *de novo* synthesis at low [OLA]/[Pb] (Figure 2B) at a variety of temperature. A standard Arrhenius plot of the logarithm of initial rates versus inverse temperature (Figure 2C) demonstrates that the activation energies for the direct transformation and the low [OLA]/[Pb] synthesis cannot be distinguished within standard error. This observation supports the idea that both reactions occur via the same mechanism.

Kinetic analysis for *de novo* nucleation and growth of 2 D perovskite nanosheets
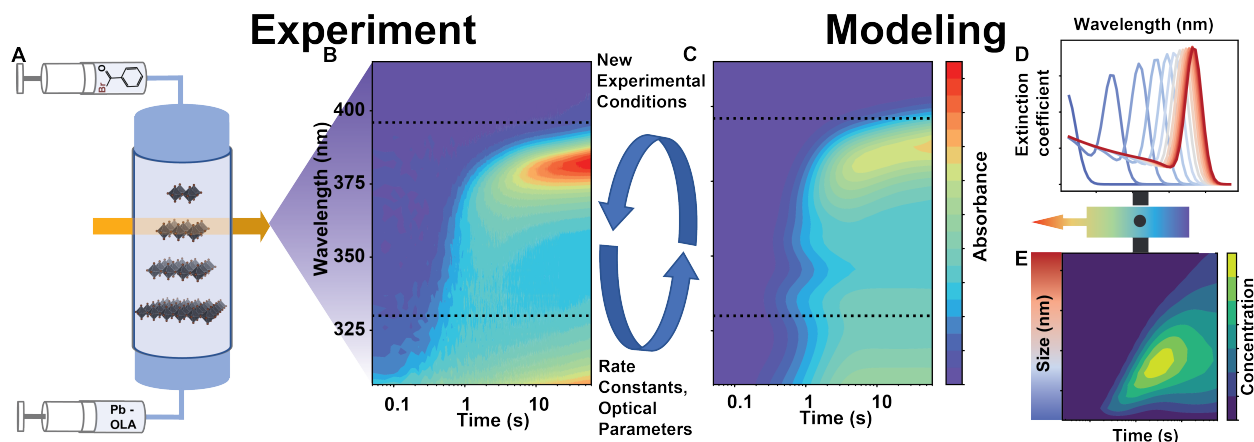

Figure 3: *Overview of Combined Model* A) Stopped flow scheme mixing benzoyl bromide and lead ions with oleylamine in a transparent window to observe nanosheet formation. B) Example of time series of absorption spectra obtained from stopped flow measurements. C) Example of time series of absorption spectra obtained from combined model and fit to data in B. D) Optical model of extinction coefficient as a function of particle size (blue - small to red - large). E) Kinetic model of the concentration of nanosheets of different sizes as a function of time.

In the exfoliation mechanism, the concentration of nanocrystals was directly related to absorption intensity, allowing estimation of rates and activation energies based on initial rate fits to kinetic measurements. In a nucleation and growth mechanism, such measurements are not possible because a wide distribution of particle sizes are present simultaneously. Since confinement effects mean that the wavelength of the excitonic absorption peak depends on particle size, concentrations of nanoparticles with a wide size distribution cannot be extracted simply from the absorption intensity. To extract growth kinetics and mechanistic information from the time-dependent spectrum, we developed a combined kinetic and spectral model to predict both the particle-size distribution and corresponding absorption spectrum as a function of time. We optimised the parameters of this model to reproduce our experimental data and hence determined the likely range of kinetic parameters for nanocrystal nucleation. This process is shown schematically in Figure 3.

Exciton Energy Model

The first component of the combined model is a description of how the excitonic energy (i.e. the absorption frequency) depends on particle size, based on time-dependent quantum mechanical calculations. The OLA_2PbBr_4 nanosheet was simulated via a tight-binding GW-BSE method[34] summarized in the SI. The tight-binding nature of the method enables us to calculate the optical gaps and band gaps as a function of the nanosheet size. The GW approximation is applied to correct the underestimated DFT band gap, followed by the Bethe-Salpeter Equation (BSE) to calculate the excitonic energy. Since the largest nanosheet that was computationally tractable with the tight-binding GW-BSE was 15.3 nm for the band gap and 4.1 nm for the optical gap, we fitted an effective mass model to the calculated values to estimate the optical gap of larger nanosheets.

We model the band gap of a nanosheet, E_G^{NS}, as the sum of the band gap of an infinite two-dimensional OLA_2PbBr_4 slab, E_G^{2D}, and the confinement energy of the electron and hole, $E_{conf,e}$ and $E_{conf,h}$.

$$E_G^{NS} = E_G^{2D} + E_{conf,e} + E_{conf,h} \tag{1}$$

Similarly, the optical gap of a nanosheet, E_{opt}^{NS}, is modeled as a sum of the optical gap of an infinite slab, E_{opt}^{2D} composed of the energy of the gap of the 2D material E_G^{2D} and the 2D exciton binding energy E_b^{2D}, as well as the confinement energy of an exciton, $E_{conf,X}$.

$$E_{opt}^{NS} = E_{opt}^{2D} + E_{conf,X} = E_G^{2D} - E_b^{2D} + E_{conf,X} \tag{2}$$

When an exciton in a nanosheet is approximated as a particle in a simple two dimensional box, $E_{conf,X}$ is proportional to $\frac{1}{m_p L^2}$ where m_p is the effective mass of a quasi particle p and L is the side length of the nanosheet. However, a classical effective mass model with $\frac{1}{L^2}$-dependence was unable to fit the tight-binding GW-BSE energies, even when the effective masses of electron and hole were treated as separate free parameters. Good fits to GW-BSE energies for both optical gaps and band gaps were obtained using a $\frac{1}{L}$ dependence for $E_{conf,X}$.

14

These fitting parameters for this model are E_G^{2D}, E_b^{2D}, and a variable M with units of $\frac{eV}{nm}$ which replaces the effective mass dependence to allow a $\frac{1}{L}$ model (see Figure S12). Such deviation from the $1/L^2$-dependence for the excitonic energy has been observed in other nanoscale systems.[35] Assuming the mass of the exciton $m_{Exc} = m_e + m_h \approx 2m_e$ and that the free variable follows this relationship $M_{Exc} \approx 2M$, this approach leads to the following final equations:

$$E_G^{NS}(L) = E_G^{2D} + 2\frac{M}{L} \tag{3}$$

$$E_{opt}^{NS}(L) = E_G^{2D} - E_b^{2D} + \frac{M}{2L} \tag{4}$$

These two equations were jointly fit to the calculated band gaps $E_G^{NS}(L)$ and optical gaps $E_{opt}^{NS}(L)$ to determine the three parameters. The optical gap of an infinite two dimensional slab E_{opt}^{2D} is estimated to be 3.03 eV based on this fit, which is in line with the experimental measurements on the emission energy of micron-scale single layer $(C_4H_9NH_3)_2PbBr_4$ crystals.[36]

Spectral Model

Next, we modified a model from Sun and Goldys[37] to allow estimation of the excitonic peak extinction coefficients and peak widths as a function of lateral plate size. The original model assumed a gaussian distribution of plate sizes centered on L and with width σ_L. This distribution produces an estimated optical exciton peak width, W_{opt}^{NS}, for a nanosheet, given by:

$$W_{opt}^{NS}(L) \sim \frac{\partial E_{opt}^{NS}(L)}{\partial L}\frac{1}{\sigma_L} \tag{5}$$

Similarly, the extinction coefficient ϵ^{NS} is given by

$$\epsilon^{NS}(L) \sim \frac{1}{E_{opt}^{NS}(L)}\frac{1}{W_{opt}^{NS}(L)} \tag{6}$$

Into these expressions we substitute the approximation for the exciton energy that was fitted to the DFT values (eq. (4)). Since the material at large L is a 2D material with a strong exciton binding energy and clearly distinguishable exciton peak, we also add constant infinite 2D slab exciton linewidths B and extinction coefficients D as fit parameters, as in the original model both linewidth and extinction vanish with increasing size. In addition, we assume that individual plates have discrete side lengths given by integer multiples of the width of a unit cell, $\Delta L = 0.45$ nm. This assumption is also used in the kinetic model. We therefore approximate $\sigma_L \approx \frac{\Delta L}{L}$, to account for errors arising from the assumption that only square plates with integer numbers of unit cells $L \pm \Delta L$ are formed, while in reality a variety of plates with different numbers of adatoms may exist. Combining these substitutions, we arrive at the usable expressions:

$$W_{opt}^{NS}(L) = A\frac{M\Delta L}{2L} + B \tag{7}$$

$$\epsilon^{NS}(L) = C\frac{1}{A\frac{M\Delta L}{2L} + B} * \frac{1}{E_G^{2D} - E_b^{2D} + \frac{M}{2L}} + D \tag{8}$$

where A and C denote fit parameters substituted for the material properties used by Sun and Goldys that have not been determined for this system.

We model the excitonic peak as a gaussian function, with the center given by the exciton energy model eq.(4), and the exciton extinction coefficient and peak width determined by the above equations. To this gaussian, we add a power law, with two fit variables F and H, to describe the distribution of states above the bandgap ($S > G$):

$$\epsilon^{S>G}(\lambda) = \begin{cases} F\lambda^H, & \text{if } \lambda < E_{opt}^{NS}(L) \\ 0, & \text{if } \lambda \geq E_{opt}^{NS}(L) \end{cases} \tag{9}$$

Experimental spectra can be described sufficiently by this model by summing over all side lengths based on the concentration C_L of each nanosheet:
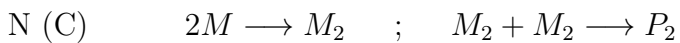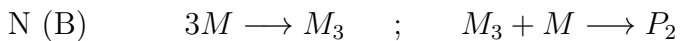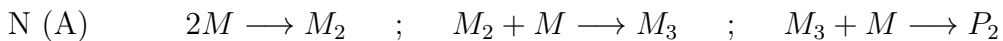
$$\epsilon(\lambda) = \sum_L C_L[\epsilon^{NS}(L) * e^{(\frac{\lambda - E_{opt}^{NS}(L)}{W_{opt}^{NS}(L)})^2} + \epsilon^{S>G}(\lambda)] \tag{10}$$

On all of the free parameters involved in the spectral model, we imposed limits based on spectra of large $OLA_2 PbBr_4$ nanosheets in solution, coupled with ICP measurements of Pb concentrations.

Kinetic Model

The preceding sections provide simple equations to convert a predicted nanosheet size distribution into a model absorption spectrum. To predict these distributions theoretically, we constructed a series of time-dependent models for plate formation and growth, each corresponding to a different growth mechanism. By comparing to the experimental spectra, we are able to discriminate between these different mechanisms and identify the most probable.

We chose a simple description of nanosheets as square arrays of unit cells with the thickness of a single cell and a side length of N unit cells. We assume that these plates nucleate from collision of monomer units that form in solution, with a minimum stable nucleus size $N = 2$ (i.e. 4 monomer units). We consider the following three possible nucleation mechanisms, where M_n indicates a cluster of n monomers and P_2 indicates the minimum stable nucleus:

N (A) $\qquad 2M \longrightarrow M_2 \quad ; \quad M_2 + M \longrightarrow M_3 \quad ; \quad M_3 + M \longrightarrow P_2$

N (B) $\qquad 3M \longrightarrow M_3 \quad ; \quad M_3 + M \longrightarrow P_2$

N (C) $\qquad 2M \longrightarrow M_2 \quad ; \quad M_2 + M_2 \longrightarrow P_2$

Similar to Riedinger et al.,[38] we use the assumption that nanosheet growth is rate-limited by nucleation of new facets (or in this purely 2D case, edge layers). Using this assumption, all nanosheets grow and shrink laterally using the same set of equations. We created multiple models based on different mechanistic possibilities:

1. Either one or two monomer units could be involved in the nucleation of new edges,

depending on whether the rate limiting step is the attachment of the first monomer to the plate, or the formation of a linear cluster on the plate edge.

2. Attachment for new monomers on a plate rates could depend linearly on the number of edge atoms in a plate (4N - 4) (i.e. the attachment to an edge site is rate limiting), or they could be constant with plate size (i.e. diffusion of monomers to the plate is limiting).

These different possibilities may all be described by the following differential equation for P_N, the concentration of plates with side length N:

$$
\begin{aligned}
\frac{d[P_N]}{dt} =\ & k_{attach} \times [P_{N-1}][M]^a (4(N-1) - 4)^b \\
& - k_{attach} \times [P_N][M]^a (4N - 4)^b \\
& - k_{detach} \times [P_N] \\
& + k_{detach} \times [P_{N+1}].
\end{aligned}
\tag{11}
$$

Here, $[M]$ is the concentration of monomers and a, b are exponents that codify different choices for the above mechanistic possibilities: $a = 1$ or 2 and $b = 0$ or 1. A cartoon depiction of each of these mechanisms can be found in Figure 4 E.

Combining the different mechanistic possibilities for nucleation with the different choices of exponents in the growth equation, we consider a total of 12 different reaction networks. Each possibility is combined with a simple kinetic treatment of the key solution-phase reactions, such as the decomposition of benzoyl bromide and formation of lead halide complexes. Utilizing a modified Runge-Kutta method implemented in Fortran, we were able to numerically solve the resulting differential equations for a range of model parameters (i.e. rate constants) and predict time series of every species' concentrations as well as particle size distributions varying through time. Further information can be found in the SI.

Optimization Process

By multiplying the simulated concentration of each plate size at each point in time with the appropriate extinction coefficient for that plate size, we can effectively simulate the stopped flow spectra. To determine the optimal fitting parameters for our various models, we defined a local loss function $\chi^2_{I_{tot}} = \sum_{i,t,\lambda}(I_{i,t,\lambda} - S_{i,t,\lambda})^2/\sigma^2_{i,t,\lambda}$, where $I_{i,t,\lambda}$ are the experimentally measured absorbance values for each experiment i, time t and wavelength λ, the corresponding standard deviation of measured values is $\sigma_{i,t,\lambda}$, and $S_{i,t,\lambda}$ represents the simulated stopped flow data. We constructed a global loss function by adding the χ^2 loss of all absorbance values in the nanosheet range (305-420 nm) to the χ^2 loss of the exciton energy peak position (λ_{max}) and height (I_{max}), determined as the highest intensity peak above 350 nm with absorbance greater than 20 mAu. This procedure was useful to improve optimization for misaligned peaks and to avoid local optima with no discernible exciton absorbance. In addition, we added a penalty for solutions that did not produce nanosheets with side lengths greater than 4 unit cells, which was the critical nucleus size observed in our simulations, or that took longer than 20 s to calculate.

$$Loss = \chi^2_{I_{tot}} + \chi^2_{\lambda_{max}} + \chi^2_{I_{max}} + \sum_{N=1}^{4}[P_N]/\sum_{N=4}^{N_{max}}[P_N] + \text{Time Penalty} \qquad (12)$$

To minimize this function and determine the rate constants of the kinetic model and the optical parameters in the spectral model within physically reasonable bounds, we used a differential evolution algorithm[39] for each of the 12 potential mechanisms. In each generation of the algorithm, the quality of fit for a population of ~ 200 parameter sets was evaluated according to equation 12, then a set of new models was generated by adding a fraction of each of the other models to the best model. The fraction that each model contributed to the respective perturbation of the best model depended on the relative quality of its fit.

We validated these results using an extrapolative cross-validation and testing regime. We constructed a series of test models by fitting the first 400 data points from 3 randomly-

selected stopped flow experiments (out of 9 performed in total), and examined their ability to predict the remaining experiments. The test set also included two additional experiments that were never used in training, one of which had a value of bromide precursor 3 times higher than any other experiment (Figure 4B). This testing framework allowed reasonable comparison of the models across experimental conditions with different benzoyl bromide, oleylamine and lead oleate concentrations. Such an extrapolative cross-validation procedure would not be useful in a traditional machine learning context, where extrapolation is frequently not possible and model training is relatively cheap. In our case, the physical nature of the models makes extrapolative predictions possible while training many models requires significant computational expense.

Analysis of combined model results

Our optimised models were able to reproduce important features of the spectra qualitatively, such as the peak wavelength evolution (Compare Figure 4A and 4B). The simulated stopped flow experiments correctly reproduce the appearance of the exciton peak at ~ 0.2 seconds, the observed blueshift of peak wavelengths at the onset ($\sim 370 - 380$ nm), and the growth and redshift of the exciton peak between 0.2 and 1 seconds. The ability to connect spectral features with evolution of the particle size distribution confirms our expectation that these three features correspond to the accumulation of critical nuclei, the formation of small, blue-shifted nanosheets, and the gradual growth of nanosheets which relaxes optical confinement, respectively. This qualitative agreement is in contrast to randomly guessed parameters - even a large initial array of hundreds of randomly chosen parameters rarely allows for any significant generation of nanosheets, much less the replication of gradual growth observed here. Most crucially, while all of the models can at least somewhat fit the overall data they were trained on, most of them cannot perform any extrapolation (Figure 4 F), and can thus be discarded. The reaction with nucleation mechanism N (A) and a layer nucleation that is linearly dependent on the number of edge units of a plate and second order with
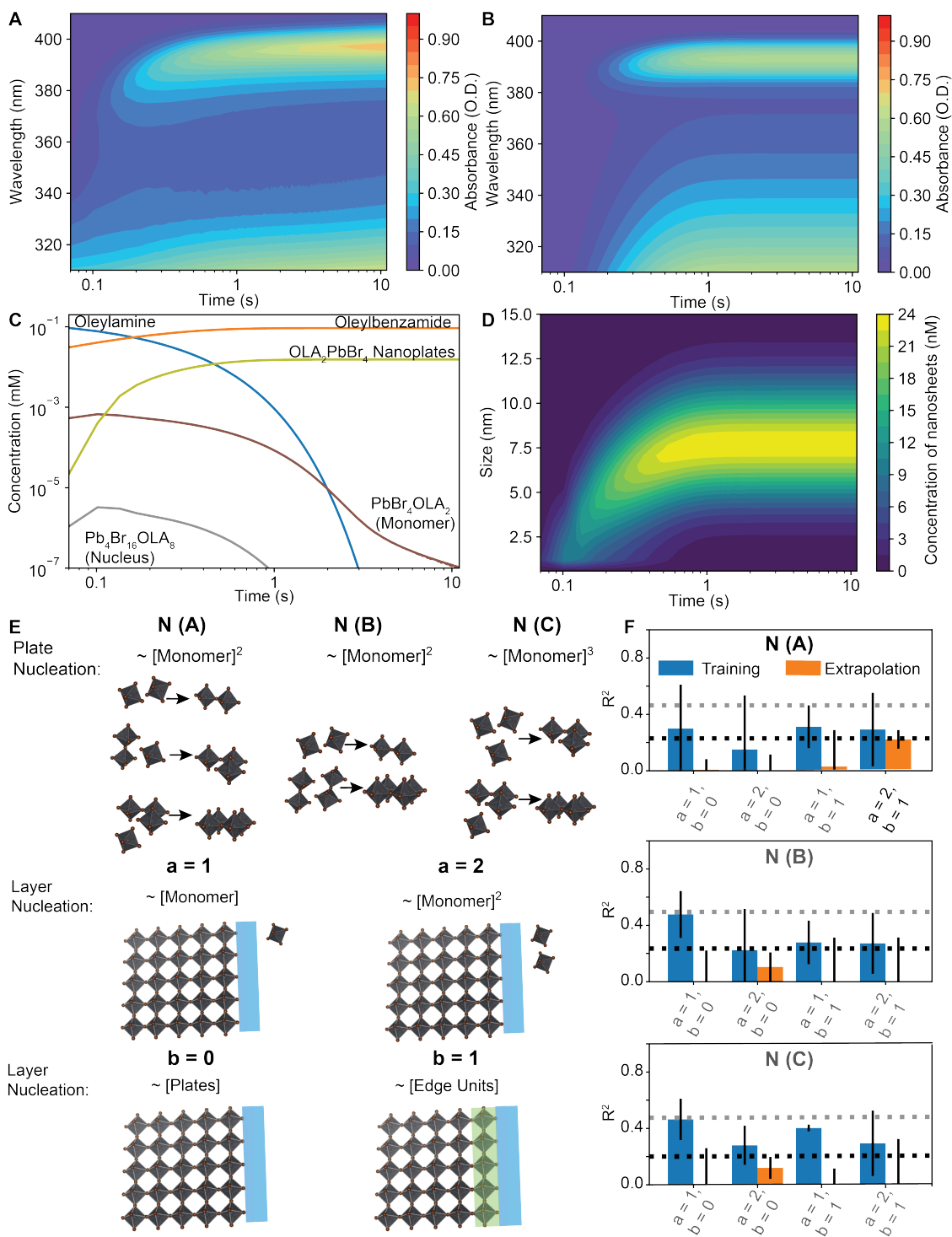
Figure 4: *Extrapolation from Optimized Combined Model* A) Experimental stopped flow results for extrapolation tests of observed synthesis dynamics at bromide concentrations higher than any in the trained dataset. B) Predicted stopped flow results at identical conditions based on training set. C) Time traces of concentrations of simulation in B. D) Particle size distribution as a function of time in simulation in B. E) Cartoon reactions of differing reactions utilized in models. F) Summary of model performance for a combinatorial combination of all reactions shown in E, evaluated through cross-validated extrapolation testing. Each panel represents results from a different nucleation mechanism, while bars represent different growth mechanisms

respect to the concentration of monomer units has the best relative ability to extrapolate to new conditions. Given the overall quality of fit, we are somewhat cautious about final conclusions as to which mechanism is operating in this reaction. As with all disproof-based mechanistic validation, we can only say that it is more likely than the other mechanisms we have proposed.
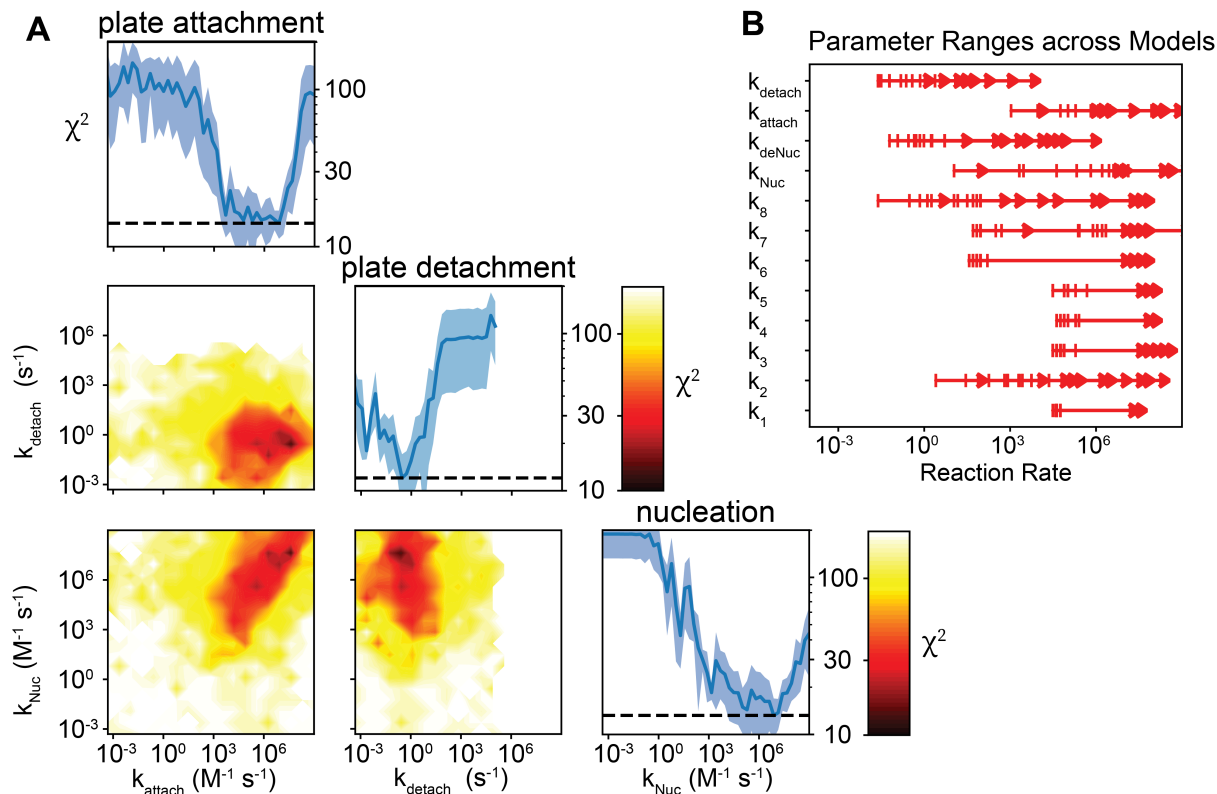

Figure 5: *Parameter Determination* A) Single Variable (Diagonal, blue) and Dual Variable (Lower left corner) plots of changes in overall fit value with changes in Plate attachment k_{attach}, Plate detachment k_{detach} and Nucleation rate k_{Nuc} B) Parameter regimes yielding best fits across multiple mechanistic models. Each row corresponds to a model parameter (k_1 through k_8 are rate constants for various solution reactions). On each row, a series of maplet arrows indicate the range of values that parameter may take without significantly worsening the fit of a corresponding model, with each range starting with a line and ending in an arrow. Specifically, these ranges correspond to the parameter regime in which the shaded region of the single variable plot in A) falls below the best average fit value (dotted black line).

The sensitivity of the loss function to a particular parameter is somewhat conserved

across multiple models where other parameters may vary, which can give insight into which parameters most control the observed behaviour. Unsurprisingly, plate and layer nucleation rates and denucleation rates significantly affect how well the simulation fits the data (Figure 5 A) - raising the relative χ^2 by more than an order of magnitude, which suggests that they are the controlling steps in this process. The nucleation rate appears to be fast relative to growth rates (Factor of 100:1), suggesting that LaMer-type reaction models of fast nucleation and slow growth[40–42] may apply to 2D perovskite nanosheets. There appears to be a correlation between plate and layer nucleation, i.e. reasonable fits could be obtained by increasing or decreasing both rate constants while keeping the ratio between them constant (Bottom left panel of figure 5 A). As the particle size distribution of nanosheets depends largely on the ratio between nucleation and growth rate,[41,42] this observation suggests that there is a unique size distribution that corresponds to the observed width of the exciton peak.

The rate of monomer detachment from the plate did not appear to correlate with either plate or layer nucleation, and good fits required it to be 3-5 orders of magnitudes slower than nucleation and growth rates across a variety of models (Figure 5 B), suggesting that it plays at most a minor role in the overall reaction dynamics. This suggests that even though growth slows down on the order of seconds to minutes, Ostwald ripening does not play an important role for nanoplate growth on this timescale. We did not observe a strong sensitivity to the optical fit parameters, except for the overall extinction coefficient, which scales with the magnitude of the absorbed intensity.

Most solution-phase rate constants did not affect the quality of the final fit results even when varied over a wide parameter regime, as long as they did not fall below a certain critical value (usually $10^4 \text{s}^{-1} \text{mM}^{-1}$). This is true even if different nucleation and growth models are utilized - see Figure 5 B, where many models show similar upper and lower limits for some solution reaction rates. This invariance indicates that solution reactions are fast compared to the rate determining step in the model, which is most likely the plate attachment rate.

The parameter sensitivity analysis determines a set of general design rules for generating 2D nanoplates with the mechanisms we have explored: Nucleation should be 10 - 100 times faster than plate attachment, while layer detachment should be 1000 - 100,000 times slower than layer attachment. Deviation from these ratios most often resulted in simulations in which no nanoplates at all were formed, or in which all nanoplates remained as nuclei.

Quantitatively, the models correlate with the overall spectral values of all the reactions observed after a joint fit to only one third of the reactions. Our approach shows that there are some rates which are similar across different mechanisms, or kept in a certain ratio to qualitatively match the observed experimental spectra. We can also confine the rates for most of the reactions to 2-3 orders of magnitude from a search space of 10 orders of magnitude. Given that we fit at least 10 physical parameters in each model, this amounts to a reduction of the multidimensional possible parameter space to a fraction of less than one millionth of the original search space. However, the somewhat low R^2 (≤ 0.5) and high χ^2 (≥ 12) values for the training sets suggest there is still some portion of the physics which is not captured appropriately. Further optimization and refinement of the kinetic models may allow more robust disproof-based choice of a reaction mechanism in the future.

Our results demonstrate that it is possible to create mechanistic models of 2D nanomaterial formation and fit them to observed data. More generally, given a reasonable theoretical description of the measurement, a mechanistic model can be fitted directly to the observed data even if crucial physical parameters, such as the size-dependent extinction coefficient, are not known. Furthermore, being able to extrapolate to new chemical parameter regimes from the given model presents an advantage over more traditional machine learning methods. This technique could in principle be applied to any nanomaterials synthesis where in-situ data can be collected.[43] In future, melding machine learning and traditional modeling techniques may enable better understanding and prediction of materials chemistry systems and allow creation of better materials through rational synthesis.

Conclusion

We obtained in-situ optical data of a 2D perovskite nanosheet synthesis with high time resolution and over a wide compositional range. We demonstrated that there are two formation pathways for this nanoscale species: chemical exfoliation and direct nucleation. These pathways can be controlled through the ratio of oleylamine to lead in the synthesis. Transformation reactions from synthesized $PbBr_2$ nanocrystals with oleylammonium bromide have similar activation energies as synthesis occuring at low oleylamine to lead ratios, further supporting the exfoliation synthesis mechanism. We have complemented traditional kinetic analysis techniques by developing a physically interpretable scientific machine learning model composed of a spectral and a kinetic component, that can be fitted directly to observed stopped-flow data and that allows extrapolative prediction of experiments with conditions differing significantly from the training dataset. This approach is in principle amenable to active learning campaigns that iteratively refine the models of nanoplate formation through performing and analyzing kinetic experiments, which would enable inference of processes involved in nanocrystal formation or other complex chemical systems through disproof-based modeling.[44] The framework that we advocate here fits neatly into the gap between traditional physical modeling and machine learning and could be useful for understanding and predicting synthesis problems more generally.

References

(1) Ahneman, D. T.; Estrada, J. G.; Lin, S.; Dreher, S. D.; Doyle, A. G. Predicting reaction performance in C–N cross-coupling using machine learning. *Science* **2018**, *360*, 186–190.

(2) Zahrt, A. F.; Henle, J. J.; Rose, B. T.; Wang, Y.; Darrow, W. T.; Denmark, S. E. Prediction of higher-selectivity catalysts by computer-driven workflow and machine learning. *Science* **2019**, *363*.

(3) Granda, J. M.; Donina, L.; Dragone, V.; Long, D.-L.; Cronin, L. Controlling an organic synthesis robot with machine learning to search for new reactivity. *Nature* **2018**, *559*, 377–381.

(4) Voznyy, O.; Levina, L.; Fan, J. Z.; Askerka, M.; Jain, A.; Choi, M.-J.; Ouellette, O.; Todorović, P.; Sagar, L. K.; Sargent, E. H. Machine Learning Accelerates Discovery of Optimal Colloidal Quantum Dot Synthesis. *ACS Nano* **2019**, *13*, 11122–11128.

(5) Braham, E. J.; Cho, J.; Forlano, K. M.; Watson, D. F.; Arròyave, R.; Banerjee, S. Machine Learning-Directed Navigation of Synthetic Design Space: A Statistical Learning Approach to Controlling the Synthesis of Perovskite Halide Nanoplatelets in the Quantum-Confined Regime. *Chemistry of Materials* **2019**, *31*, 3281–3292.

(6) Owen, J. S.; Park, J.; Trudeau, P.-E.; Alivisatos, A. P. Reaction Chemistry and Ligand Exchange at Cadmium-Selenide Nanocrystal Surfaces. *Journal of the American Chemical Society* **2008**, *130*, 12279–12281.

(7) Owen, J. S.; Chan, E. M.; Liu, H.; Alivisatos, A. P. Precursor Conversion Kinetics and the Nucleation of Cadmium Selenide Nanocrystals. *Journal of the American Chemical Society* **2010**, *132*, 18206–18213.

(8) Blackmond, D. G. Reaction Progress Kinetic Analysis: A Powerful Methodology for Mechanistic Studies of Complex Catalytic Reactions. *Angewandte Chemie International Edition* **2005**, *44*, 4302–4320.

(9) Watzky, M. A.; Finke, R. G. Transition Metal Nanocluster Formation Kinetic and Mechanistic Studies. A New Mechanism When Hydrogen Is the Reductant: Slow, Continuous Nucleation and Fast Autocatalytic Surface Growth. *Journal of the American Chemical Society* **1997**, *119*, 10382–10400.

(10) Finke, R. G.; Watzky, M. A.; Whitehead, C. B. Response to "Particle Size Is a Primary Determinant for Sigmoidal Kinetics of Nanoparticle Formation: A "Disproof" of the Finke–Watzky (F-W) Nanoparticle Nucleation and Growth Mechanism". *Chemistry of Materials* **2020**, *32*, 3657–3672.

(11) Yang, H.; Hamachi, L. S.; Rreza, I.; Wang, W.; Chan, E. M. Design Rules for One-Step Seeded Growth of Nanocrystals: Threading the Needle between Secondary Nucleation and Ripening. *Chemistry of Materials* **2019**, *31*, 4173–4183.

(12) Dahl, J. C.; Wang, X.; Huang, X.; Chan, E. M.; Alivisatos, A. P. Elucidating the Weakly Reversible Cs–Pb–Br Perovskite Nanocrystal Reaction Network with High-Throughput Maps and Transformations. *Journal of the American Chemical Society* **2020**, *142*, 11915–11926.

(13) Rackauckas, C.; Nie, Q. DifferentialEquations.jl – A Performant and Feature-Rich Ecosystem for Solving Differential Equations in Julia. *Journal of Open Research Software* **2017**, *5*.

(14) Ji, W.; Qiu, W.; Shi, Z.; Pan, S.; Deng, S. Stiff-PINN: Physics-Informed Neural Network for Stiff Chemical Kinetics. *The Journal of Physical Chemistry A* **2021**, *125*, 8098–8106.

(15) Ji, W.; Deng, S. Autonomous Discovery of Unknown Reaction Pathways from Data by Chemical Reaction Neural Network. *The Journal of Physical Chemistry A* **2021**, *125*, 1082–1092.

(16) Tsakonas, C.; Dimitropoulos, M.; Manikas, A. C.; Galiotis, C. Growth and in situ characterization of 2D materials by chemical vapour deposition on liquid metal catalysts: a review. *Nanoscale* **2021**, *13*, 3346–3373.

(17) Qin, M.; Chan, P. F.; Lu, X. A Systematic Review of Metal Halide Perovskite Crystallization and Film Formation Mechanism Unveiled by In Situ GIWAXS. *Advanced Materials* **2021**, *33*, 2105290.

(18) Hoffman, J. M.; Strzalka, J.; Flanders, N. C.; Hadar, I.; Cuthriell, S. A.; Zhang, Q.; Schaller, R. D.; Dichtel, W. R.; Chen, L. X.; Kanatzidis, M. G. In Situ Grazing-Incidence Wide-Angle Scattering Reveals Mechanisms for Phase Distribution and Disorientation in 2D Halide Perovskite Films. *Advanced Materials* **2020**, *32*, 2002812.

(19) Sadighian, J. C.; Wong, C. Y. Just Scratching the Surface: In Situ and Surface-Specific Characterization of Perovskite Nanocrystal Growth. *The Journal of Physical Chemistry C* **2021**, *125*, 20772–20782.

(20) Pradhan, N. Growth of Lead Halide Perovskite Nanocrystals: Still in Mystery. *ACS Physical Chemistry Au* **2022**, acsphyschemau.2c00001.

(21) Saparov, B.; Mitzi, D. B. Organic–Inorganic Perovskites: Structural Versatility for Functional Materials Design. *Chemical Reviews* **2016**, *116*, 4558–4596.

(22) Hong, X.; Ishihara, T.; Nurmikko, A. V. Dielectric confinement effect on excitons in PbI4 -based layered semiconductors. *Physical Review B* **1992**, *45*, 6961–6964.

(23) Mitzi, D. B.; Chondroudis, K.; Kagan, C. R. Organic-inorganic electronics. *IBM Journal of Research and Development* **2001**, *45*, 29–45.

(24) Novoselov, K. S.; Mishchenko, A.; Carvalho, A.; Neto, A. H. C. 2D materials and van der Waals heterostructures. *Science* **2016**, *353*.

(25) Udayabhaskararao, T.; Houben, L.; Cohen, H.; Menahem, M.; Pinkas, I.; Avram, L.; Wolf, T.; Teitelboim, A.; Leskes, M.; Yaffe, O.; Oron, D.; Kazes, M. A Mechanistic Study of Phase Transformation in Perovskite Nanocrystals Driven by Ligand Passivation. *Chemistry of Materials* **2018**, *30*, 84–93.

(26) Liu, F.; Ding, C.; Zhang, Y.; Ripolles, T. S.; Kamisaka, T.; Toyoda, T.; Hayase, S.; Minemoto, T.; Yoshino, K.; Dai, S.; Yanagida, M.; Noguchi, H.; Shen, Q. Colloidal Synthesis of Air-Stable Alloyed CsSn 1– x Pb x I 3 Perovskite Nanocrystals for Use in Solar Cells. *Journal of the American Chemical Society* **2017**, *139*, 16708–16719.

(27) Palazon, F.; Urso, C.; Trizio, L. D.; Akkerman, Q.; Marras, S.; Locardi, F.; Nelli, I.; Ferretti, M.; Prato, M.; Manna, L. Postsynthesis Transformation of Insulating Cs 4

PbBr 6 Nanocrystals into Bright Perovskite CsPbBr 3 through Physical and Chemical Extraction of CsBr. *ACS Energy Letters* **2017**, *2*, 2445–2448.

(28) Bera, S.; Behera, R. K.; Adhikari, S. D.; Guria, A. K.; Pradhan, N. Equilibriums in Formation of Lead Halide Perovskite Nanocrystals. *The Journal of Physical Chemistry Letters* **2021**, *12*, 11824–11833.

(29) Bekenstein, Y.; Koscher, B. A.; Eaton, S. W.; Yang, P.; Alivisatos, A. P. Highly Luminescent Colloidal Nanoplates of Perovskite Cesium Lead Halide and Their Oriented Assemblies. *Journal of the American Chemical Society* **2015**, *137*, 16008–16011.

(30) Protesescu, L.; Yakunin, S.; Bodnarchuk, M. I.; Krieg, F.; Caputo, R.; Hendon, C. H.; Yang, R. X.; Walsh, A.; Kovalenko, M. V. Nanocrystals of Cesium Lead Halide Perovskites (CsPbX3, X = Cl, Br, and I): Novel Optoelectronic Materials Showing Bright Emission with Wide Color Gamut. *Nano Letters* **2015**, *15*, 3692–3696.

(31) Almeida, G.; Goldoni, L.; Akkerman, Q.; Dang, Z.; Khan, A. H.; Marras, S.; Moreels, I.; Manna, L. Role of Acid–Base Equilibria in the Size, Shape, and Phase Control of Cesium Lead Bromide Nanocrystals. *ACS Nano* **2018**, *12*, 1704–1711.

(32) Hassan, Y.; Song, Y.; Pensack, R. D.; Abdelrahman, A. I.; Kobayashi, Y.; Winnik, M. A.; Scholes, G. D. Structure-Tuned Lead Halide Perovskite Nanocrystals. *Advanced Materials* **2016**, *28*, 566–573.

(33) Ahmad, S.; Kanaujia, P. K.; Niu, W.; Baumberg, J. J.; Prakash, G. V. In Situ Intercalation Dynamics in Inorganic–Organic Layered Perovskite Thin Films. *ACS Applied Materials & Interfaces* **2014**, *6*, 10238–10247.

(34) Cho, Y.; Berkelbach, T. C. Optical Properties of Layered Hybrid Organic–Inorganic Halide Perovskites: A Tight-Binding GW-BSE Study. *The Journal of Physical Chemistry Letters* **2019**, *10*, 6189–6196.

(35) Blancon, J.-C. et al. Scaling law for excitons in 2D perovskite quantum wells. *Nature Communications* **2018**, *9*, 2254.

(36) Dou, L.; Wong, A. B.; Yu, Y.; Lai, M.; Kornienko, N.; Eaton, S. W.; Fu, A.; Bischak, C. G.; Ma, J.; Ding, T.; Ginsberg, N. S.; Wang, L.-W.; Alivisatos, A. P.; Yang, P. Atomically thin two-dimensional organic-inorganic hybrid perovskites. *Science* **2015**, *349*, 1518–1521.

(37) Sun, J.; Goldys, E. M. Linear Absorption and Molar Extinction Coefficients in Direct Semiconductor Quantum Dots. *The Journal of Physical Chemistry C* **2008**, *112*, 9261–9266.

(38) Riedinger, A.; Ott, F. D.; Mule, A.; Mazzotti, S.; Knüsel, P. N.; Kress, S. J.; Prins, F.; Erwin, S. C.; Norris, D. J. An intrinsic growth instability in isotropic materials leads to quasi-two-dimensional nanoplatelets. *Nature Materials* **2017**, *16*, 743–748.

(39) Storn, R.; Price, K. Differential Evolution – A Simple and Efficient Heuristic for global Optimization over Continuous Spaces. *Journal of Global Optimization* **1997**, *11*, 341–359.

(40) LaMer, V. K.; Dinegar, R. H. Theory, Production and Mechanism of Formation of Monodispersed Hydrosols. *Journal of the American Chemical Society* **1950**, *72*, 4847–4854.

(41) Sugimoto, T. Spontaneous nucleation of monodisperse silver halide particles from homogeneous gelatin solution I: silver chloride. *Colloids and Surfaces A: Physicochemical and Engineering Aspects* **2000**, *164*, 183–203.

(42) Chu, D. B. K.; Owen, J. S.; Peters, B. Nucleation and Growth Kinetics from LaMer Burst Data. *The Journal of Physical Chemistry A* **2017**, *121*, 7511–7517.

(43) Akkerman, Q. A.; Nguyen, T. P. T.; Boehme, S. C.; Montanarella, F.; Dirin, D. N.; Wechsler, P.; Beiglböck, F.; Rainò, G.; Erni, R.; Katan, C.; Even, J.; Kovalenko, M. V. Controlling the nucleation and growth kinetics of lead halide perovskite quantum dots. *Science* **2022**, *377*, 1406–1412.

(44) Handwerk, D. R.; Shipman, P. D.; Whitehead, C. B.; Özkar, S.; Finke, R. G. Mechanism-Enabled Population Balance Modeling of Particle Formation en Route to Particle Average Size and Size Distribution Understanding and Control. *Journal of the American Chemical Society* **2019**, *141*, 15827–15839.

Graphical TOC Entry